

# Preclinical Evaluation of IMGC936, a Next-Generation Maytansinoid-based Antibody-drug Conjugate Targeting ADAM9-expressing Tumors



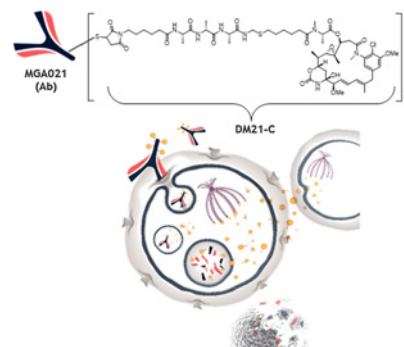
Juniper A. Scribner<sup>1</sup>, Stuart W. Hicks<sup>3</sup>, Kerstin W. Sinkevicius<sup>3</sup>, Nicholas C. Yoder<sup>3</sup>, Gundo Diedrich<sup>2</sup>, Jennifer G. Brown<sup>2</sup>, Jacquelynn Lucas<sup>3</sup>, Megan E. Fuller<sup>3</sup>, Thomas Son<sup>1</sup>, Anahita Dastur<sup>3</sup>, Jeff Hooley<sup>1</sup>, Christopher Espelin<sup>3</sup>, Marian Themeles<sup>3</sup>, Francine Z. Chen<sup>1</sup>, Ying Li<sup>1</sup>, Michael Chiechi<sup>1</sup>, Jenny Lee<sup>3</sup>, Bhaswati Barat<sup>2</sup>, Lusiana Widjaja<sup>2</sup>, Sergey Gorlatov<sup>2</sup>, James Tamura<sup>2</sup>, Valentina Ciccarone<sup>2</sup>, Olga Ab<sup>3</sup>, Kerry A. McEachem<sup>3</sup>, Scott Koenig<sup>2</sup>, Eric H. Westin<sup>2</sup>, Paul A. Moore<sup>2</sup>, Thomas Chittenden<sup>3</sup>, Richard J. Gregory<sup>3</sup>, Ezio Bonvini<sup>2</sup>, and Deryk Loo<sup>1</sup>

## ABSTRACT

ADAM metallopeptidase domain 9 (ADAM9) is a member of the ADAM family of multifunctional, multidomain type 1 transmembrane proteins. ADAM9 is overexpressed in many cancers, including non-small cell lung, pancreatic, gastric, breast, ovarian, and colorectal cancer, but exhibits limited expression in normal tissues. A target-unbiased discovery platform based on intact tumor and progenitor cell immunizations, followed by an IHC screen, led to the identification of anti-ADAM9 antibodies with selective tumor-versus-normal tissue binding. Subsequent analysis revealed anti-ADAM9 antibodies were efficiently internalized and processed by tumor cells making ADAM9 an attractive target for antibody-drug conjugate (ADC) development. Here, we describe the preclinical evaluation of IMGC936, a novel ADC targeted against ADAM9. IMGC936 is comprised of a high-affinity humanized antibody site-specifically conjugated to DM21-C, a next-generation linker-payload that combines a maytansinoid microtubule-disrupting payload with a stable tripeptide linker, at a drug antibody ratio of approximately 2.0. In addition, theYTE mutation (M252Y/S254T/T256E) was introduced into the CH2 domain of the antibody Fc to maximize *in vivo* plasma half-life and exposure. IMGC936 exhibited cytotoxicity toward ADAM9-positive human tumor cell lines, as well as bystander killing, potent antitumor activity in human cell line-derived xenograft and patient-derived xenograft tumor models, and an acceptable safety profile in cynomolgus monkeys with favorable pharmacokinetic properties.

Our preclinical data provide a strong scientific rationale for the further development of IMGC936 as a therapeutic candidate for the treatment of ADAM9-positive cancers. A first-in-human study of IMGC936 in patients with advanced solid tumors has been initiated (NCT04622774).

### IMGC936: ADAM9 Targeting ADC



- DM21-C linker-payload: improved plasma stability, facilitation of bystander killing
- CYSMAB: C442 site-specific DAR=2 conjugation
- YTE mutation in Fc to extend half-life

## Introduction

ADAM metallopeptidase domain 9 (ADAM9) is a member of the ADAM family of multifunctional, multidomain type 1 transmembrane

proteins. ADAM9, as with other members of the family, is comprised of a pro-domain, metalloprotease domain, a disintegrin domain, a cysteine-rich region, an EGF-like domain, a transmembrane domain, and a short cytoplasmic domain. In general, two biological activities have been described for ADAM9—proteolysis (via the metalloprotease domain) and adhesion (via the disintegrin domain). These functional activities of ADAM9 have been implicated in several cellular processes, including myogenesis, fertilization, cell migration, immune response, proliferation, and cell-cell and cell-matrix interactions (1). In the context of cancer, the biological activities of ADAM9 play a role in cancer formation and progression (2–7).

ADAM9 is overexpressed in malignant tumors, with limited expression in normal tissues, making it an attractive candidate for antibody-drug conjugate (ADC) targeted therapy. Overexpression of ADAM9 has been described in breast cancer (8), pancreatic ductal adenocarcinoma (9, 10), gastric cancer (11), non-small cell lung cancer (NSCLC; ref. 12, 13), renal cell carcinoma (14), cervical cancer (15), prostate cancer (16), liver cancer (17, 18), glioma (19), ovarian clear

<sup>1</sup>MacroGenics, Inc., Brisbane, CA. <sup>2</sup>MacroGenics, Inc., Rockville, MD. <sup>3</sup>ImmunoGen, Inc., Waltham, MA.

**Note:** Supplementary data for this article are available at Molecular Cancer Therapeutics Online (<http://mct.aacrjournals.org/>).

J.A. Scribner and S.W. Hicks contributed equally as co-primary authors of this article.

**Corresponding Author:** Deryk Loo, MacroGenics, Inc., 3280 Bayshore Boulevard, Suite 200, Brisbane, CA 94005. Phone: 650-624-2736; Fax: 650-624-2793; E-mail: [lood@macrogenics.com](mailto:lood@macrogenics.com)

Mol Cancer Ther 2022;21:1047–59

**doi:** 10.1158/1535-7163.MCT-21-0915

©2022 American Association for Cancer Research

cell carcinoma (20), and oral squamous cell carcinoma (21). The overexpression of ADAM9 in human cancers has been correlated with higher-grade tumors, node-positive status, metastasis to distant sites, and shortened patient survival in the majority of these cancers (8–19).

ADCs seek to increase the therapeutic window of potent cytotoxic agents by linking them with monoclonal antibodies (mAb) that can selectively target and deliver the cytotoxic payload to target-bearing cells within a tumor. Selective targeting of tumors with ADCs, in theory, increases the therapeutic index by both decreasing systemic toxicity (increasing the maximum tolerated dose) while increasing efficacy by reducing the minimal effective dose. Current advances in linker and conjugation technologies, together with the emergence of payloads with diverse potencies and alternate mechanisms of action (22, 23), have provided the opportunity to further refine and optimize the therapeutic benefit of ADCs.

We have used a discovery platform based on intact tumor or progenitor cell immunizations to generate mAbs directed to cell surface targets that are overexpressed in cancer relative to normal tissues (24). Using this approach, we generated several mAbs targeting ADAM9. The differential expression of ADAM9 on tumor compared with normal tissue and the ability of antibody-ADAM9 complexes to be internalized, led us to examine the potential to target ADAM9 with an ADC. Here we report the preclinical evaluation of IMGC936, a DM21-C maytansinoid-based ADC targeting ADAM9 that has been optimized to extend exposure. IMGC936 exhibited direct *in vitro* cytotoxicity toward ADAM9-positive tumor cell lines, as well as bystander killing. Consistent with the *in vitro* activity, IMGC936 showed potent antitumor activity in cell line-derived xenograft (CDX) and patient-derived xenograft (PDX) tumor models. In addition, IMGC936 demonstrated a favorable pharmacokinetic and acceptable safety profile in cynomolgus monkeys. Our preclinical data provide strong scientific rationale for the continued development of IMGC936 as a therapeutic candidate for the treatment of ADAM9-positive cancers.

## Materials and Methods

### Generation of the lead anti-ADAM9 antibody, MGA021

Intact cell immunizations with primary human progenitor cells and primary cancer cells were employed to generate mAbs to cell surface targets (24). Human kidney epithelial progenitor cells were isolated from fetal kidney tissue and propagated for greater than 30 passages in a serum-free, low calcium-containing I3/F-based medium (25). BALB/c mice were immunized via the foot pad with intact, viable human kidney epithelial progenitor cells and Ribi adjuvant (Corixa) over a period of 3 months. Antibody titer was monitored by flow cytometry using the human kidney epithelial progenitor cells. Lymph nodes from mice exhibiting positive titers were harvested, and lymphocytes were fused with the mouse myeloma line X63-Ag8.653 (ATCC) using standard methodology. Hybridoma supernatants were screened by IHC on frozen normal human tissues (kidney, pancreas, liver, colon, heart, and lung) and tumor tissue (lung, colon, breast, esophageal, pancreatic, and head and neck cancers) to identify mAbs with preferential binding to tumor versus normal tissue. The murine KID24 mAb was selected for further evaluation based on strong tumor versus normal IHC reactivity. Tandem mass spectrometry of protein immunoprecipitated by KID24 from A498 renal cell carcinoma cell membranes yielded a peptide corresponding to ADAM9 (Supplementary Fig. S1). An ELISA assay using recombinant human ADAM9 (R&D

Systems) confirmed that KID24 was reactive with human ADAM9, but not the related ADAM family members ADAM8, ADAM10, or ADAM17 (Supplementary Fig. S1).

The variable light chain (VL) and variable heavy chain (VH) amino acid sequences of the parental antibody, KID24, were humanized (huKID24) (Supplementary Fig. S2) using the complementary-determining region (CDR) sequences from the mouse KID24 mAb and framework sequences from human germline V-kappa or VH segment, respectively. The huKID24 VL and VH coding sequences were synthesized de novo, and fused to the human C-kappa or human gamma 1 constant region cDNA, respectively.

To improve the affinity of huKID24 toward cynomolgus ADAM9, genes were cloned into a Fab display vector (variant to pComb3X). The CDR3 region of the VH gene was randomized by replacing 6 consecutive codons (positions 100a – 100f following Kabat nomenclature) with NNS codons to allow for the inclusion of any amino acid in these positions (26). The Fab library was displayed as a pIII fusion protein on filamentous phage. Clones with improved binding to cynomolgus ADAM9 were isolated from the library by 3 rounds of affinity-based phage display panning with 20 nmol/L (round 1), 2 nmol/L (round 2), and 0.2 nmol/L (round 3) biotinylated cynomolgus ADAM9 protein (R&D Systems) immobilized on streptavidin beads (27). Clones enriched after the third round of panning were reformatted into an IgG expression plasmid and expressed in CHO cells. Surface plasmon resonance analysis identified the antibody AEX6003 as having improved binding to cynomolgus monkey ADAM9 compared with huKID24, and was selected for further engineering. Subsequently, the M252Y/S254T/T256E (YTE) triple mutation was engineered into the CH2 domain of the Fc domain and cysteine residues were substituted at position 442 of the mAb heavy chains to yield MGA021.

### Conjugation

MGA021 was reduced and reoxidized to enable site-specific conjugation at HC-C442 (Eu numbering) as described previously (28). Conjugation of MGA021 to generate IMGC936 was effected by addition of 5 equivalents of DM21-C, a maleimide-functionalized version of a previously described maytansinoid ADC linker-payload containing a tripeptide linker (29). The conjugation reaction mixture contained PBS pH 6.0 with 2 mmol/L EDTA and 10% (v:v) dimethylacetamide, and was incubated at 25°C overnight prior to purification into 10 mmol/L acetate pH 5.0 with 9% sucrose and 0.01% Tween-20. Analytical characteristics of IMGC936 are summarized in Supplementary Table S1. Drug distribution and DAR average by size exclusion chromatography-mass spectrometry for IMGC936 is shown in Supplementary Fig. S3 and Supplementary Table S2. The non-targeting control chKTI-DM21-C ADC was site-specifically conjugated at HC-C442 to an equivalent average DAR as IMGC936, as described above.

### Tumor cell lines and culture

Human tumor cell lines were obtained from the ATCC, Japanese Collection of Research Bioresources (JCRB; Sekisui XenoTech), or German Collection of Microorganisms and Cell Cultures (DSMZ). Cell lines were cultured in the medium recommended by the suppliers at 37°C in a humidified 5% CO<sub>2</sub> incubator and passaged by diluting into fresh culture medium 1 to 3 times per week to maintain a cell density between 50% and 100% confluence. The MDA-MB-468 cell line was cultured in a 0% CO<sub>2</sub> incubator. All cell lines were thawed from working cell banks, which were screened for *Mycoplasma* by PCR or using the MycoAlert Mycoplasma

Detection Kit (Lonza). Cell line authentication was confirmed by short tandem repeat profiling at ATCC, or cell lines were purchased within the period of 2010 to 2015 and authenticated by the vendor. Studies were performed with cultures that had undergone fewer than 25 passages.

ADAM9 was knocked out from the NCI-H1975 cell line using Synthego's CRISPRRevolution sgRNA EZ Kit according to the manufacturer's protocol. sgRNA was combined with Cas9 at a ratio of 1.3:1 (3  $\mu$ mol/L each) to form ribonucleoprotein particle (RNP) complexes. The RNP complexes were combined with Lipofectamine Cas9 Plus Reagent (Thermo Fisher Scientific) and Opti-MEM I Reduced Serum Media to form the RNP complex solution. This solution was incubated with Lipofectamine CRISPRMAX (Thermo Fisher Scientific) and Opti-MEM Reduced Serum Media, added to a 24-well cell culture plate, then 120,000 cells/well were added to the plate. Transfected cells were expanded for approximately 1 week then single cell sorted by flow cytometry. Individual clones were expanded for subsequent analysis to confirm human ADAM9 knockout.

ADAM9 was knocked out from the EBC-1 cell line using the CRISPR protocol from Thermo Fisher Scientific. 300,000 cells/well were plated in 6-well plates. The following day, Invitrogen TrueCut Cas9 Protein v2 and the gRNA were mixed in 1:1 ratio (37.5 pmol/L each) to form the RNP complexes then added to cells along with Opti-MEM I Reduced Serum Medium, Lipofectamine Cas9 Plus reagent and the Lipofectamine CRISPRMAX reagent. The cells were incubated at 37°C for 2 days, followed by single cell plating and expansion in 96-well plates. ADAM9 negative clones were identified by FACS.

#### **In vitro cytotoxic potency**

Assays were performed in triplicate for each data point. Tumor cells, 200 to 4,000 in 100  $\mu$ L of complete culture medium, were added to each well of flat bottom 96-well plates on Day 0. The test articles IMGC936, the non-targeting control huKTI-DM21-C, and DM50 were diluted in complete cell culture medium and 100  $\mu$ L of the dilutions were added to the plated cells the following day (Day 1). Control wells containing cells and the medium but lacking test articles, in addition to wells containing medium only, were included in each assay plate. The plates were incubated at 37°C for 5 to 6 days. The relative number of viable cells in each well was determined using the Water-Soluble Tetrazolium Salt-8 (WST-8) based Cell Counting Kit-8 (Dojindo Molecular Technologies, Inc.) according to the manufacturer's protocol. The surviving fraction of cells in each well was calculated by subtracting the average value of the wells containing medium only, and then dividing by the average value of the control wells containing cells and the medium but lacking the test articles. Concentration response curves and IC<sub>50</sub> values were generated by nonlinear regression using a sigmoidal curve fit with variable slope in Graph Pad Prism.

#### **Bystander Activity**

NCI-H1975/ADAM9 KO cells stably expressing red fluorescent protein (NCI-H1975/ADAM9 KO/RFP) were generated using the IncuCyte NucLight Red Lentivirus (Sartorius) according to the manufacturer's protocol. Parental NCI-H1975 cells (0–5,000 cells/well) were mixed with NCI-H1975/ADAM9 KO/RFP cells (5,000 cells/well) and plated in flat-bottom plates. IMGC936 (67 nmol/L) was added to plates, then plates were incubated at 37°C and cell viability of NCI-H1975/ADAM9 KO/RFP cells was measured after 5 days using an IncuCyte Live-Cell Analysis System (Sartorius).

#### **In vivo efficacy – tumor xenograft studies**

Efficacy studies and procedures were approved by MacroGenics, Inc. or ImmunoGen, Inc. Institutional Animal Care and Use Committees in accordance with the Guide for the Care and Use of Laboratory Animals (National Research Council).

Female CD-1 Nude (homozygous) mice (Crl:CD-1-*Foxn1<sup>nu</sup>*), female Athymic Nude mice (Crl:NU(NCr)-*Foxn1<sup>nu</sup>*), or female Fox Chase SCID mice (CB17/Icr-*Prkdc<sup>scid</sup>*/IcrIcoCrl) from Charles Rivers Laboratories, weighing 15 to 30 g each and 5 to 7 weeks of age, were used in the efficacy studies. Mice were maintained under pathogen-free conditions, with food and water supplied ad libitum. Human tumor cells ( $3 \times 10^6$  to  $1 \times 10^7$  viable cells) were resuspended in 1:1 serum-free medium and Matrigel Basement Membrane Matrix (Corning) and inoculated subcutaneously into the flank of CD-1 Nude (homozygous) mice (HPAF-II, SW48 cells), Athymic Nude mice (SNU-5 cells), or Fox Chase SCID mice (EBC-1, EBC-1 ADAM9 Knockout, MDA-MB-231, NCI-H1975 cells).

When tumor volumes reached approximately 100 to 150 mm<sup>3</sup>, mice were randomized into groups of 6 to 8 individuals per group and treated with test articles (ADCs, MGA021 or unconjugated payload DM50) or vehicle control [PBS or IMGC936 Formulation Buffer (10 mmol/L sodium succinate, 9% (w/v) sucrose, 0.01% polysorbate-20, pH 4.7)] intravenously (IV) by tail vein injection (100–225  $\mu$ L). Single-dose administration studies were performed with ADC doses ranging from 1.25 to 10 mg/kg depending on the study. Unconjugated antibodies were dosed at 10 mg/kg and DM50 was dosed at 100  $\mu$ g/kg (equivalent to payload present in 10 mg/kg IMGC936).

Tumors were measured twice weekly by orthogonal measurements with electronic calipers, with tumor volumes calculated as: (length  $\times$  width  $\times$  height)/2. Individual animal weights were recorded 1 to 2 times weekly beginning at the time of tumor cell inoculation and continuing until study completion.

PDX studies were performed at Champions Oncology. Female Athymic Nude-*Foxn1<sup>nu</sup>* from Envigo, 6 to 8 weeks of age, weighing at least 18 g, were used in the studies. Low passage tumor fragments were implanted into stock animals. When tumors reached 1.0 to 1.5 cm<sup>3</sup>, tumor fragments were reimplanted into pre-study animals unilaterally on the left flank. When tumors reached an average tumor volume of 150 to 300 mm<sup>3</sup>, animals were randomized by tumor volume into treatment or vehicle control groups. Three animals were assigned to each group and dosed IV by tail vein injection (100–225  $\mu$ L). Tumor volumes were measured twice weekly by calipers. Tumor volume was calculated using the formula TV = (width  $\times$  2)  $\times$  length  $\times$  0.52.

#### **Toxicology**

A nonhuman primate study was conducted using purpose-bred naïve male and female cynomolgus monkeys (*Macaca fascicularis*) of Asian origin at an Association for Assessment and Accreditation of Laboratory Animal Care International-accredited, U.S. Department of Agriculture-inspected laboratory. The study protocol was approved by the testing facility Institutional Animal Care and Use Committee. The repeat-dose toxicology study consisted of treatment groups (5 male/5 female) administered either the vehicle control (10 mmol/L sodium succinate, 9% (w/v) sucrose, 0.01% polysorbate 20, pH 4.7) or IMGC936 by IV infusion over 10 minutes, at a 2 week interval (3, 10, or 22.5 mg/kg/dose), for a total of 2 doses on days 1 and 15. Six animals per group (3/sex/group) were necropsied on day 19, while the remaining recovery group animals (2/sex/group) were necropsied on day 57 following a 6-week recovery period. Mortality, clinical signs, body weights, food consumption, and clinical pathology were

monitored prior to and throughout the study. Slit lamp biomicroscopy and indirect ophthalmoscopy was performed pre-study and prior to terminal and recovery sacrifice by a veterinary ophthalmologist. Electrocardiology was conducted pre-study for a 24-hour period and on day 15 starting 3-hours predose through 21-hours postdose using jacketed external telemetry. Respiration rate (performed cage side) and blood pressure (performed on restrained animals) were measured pre-study and on days 5 and 17. Following terminal and recovery sacrifice, gross necropsy, measurement of organ weights and histopathologic examinations were conducted. A toxicokinetic assessment was also performed.

#### Data availability statement

The data generated in this study are available within the article and its supplemental data files.

## Results

### Selection and generation of IMGC936

Immunizations with intact, viable human tumor or progenitor cells, followed by an IHC screen for cancer-specific antibody candidates, led to the identification of anti-ADAM9 mAbs with highly differential tumor-versus-normal tissue binding (Fig. 1A) (24). Preliminary screening of the anti-ADAM9 mAbs revealed that a subset of the mAbs were efficiently internalized *in vitro* by tumor cells (30), suggesting they were promising candidates for an ADC approach. To confirm and extend this observation, we assessed the antigen/antibody uptake and proteolytic processing rate of two of the lead murine anti-ADAM9 mAbs. As shown in Fig. 1B, and summarized in Supplementary Table S3, incubation of anti-ADAM9 mAbs with ADAM9-expressing tumor cells led to rapid internalization and proteolytic processing, with 50% to 90% of the mAbs processed in 24 hours (31). On the basis of the internalization/proteolytic processing data, the KID24 mAb was selected for humanization and subsequent preclinical development.

KID24 was humanized by CDR grafting (huKID24) and fused to human C-kappa and gamma 1 constant regions and retained the binding affinity of the parental murine mAb for human ADAM9. However, the binding affinity of KID24 and huKID24 was found to be nearly 100-fold lower for cynomolgus monkey ADAM9 compared with human ADAM9. Affinity optimization was undertaken to improve the binding of huKID24 for cynomolgus monkey ADAM9. Screening of a huKID24 Fab mutagenic phage library identified clone AEX6003 as having equivalent binding affinity for human and cynomolgus monkey ADAM9 (Fig. 1C).

Two additional elements were engineered into AEX6003 to generate the development candidate MGA021. First, the M252Y/S254T/T256E (YTE) triple mutation was engineered into the CH2 domain of the Fc region to improve the neonatal Fc receptor (FcRn) binding profile and optimize the pharmacokinetic properties of the mAb. The YTE triple mutation incorporated into MGA021 improved binding to human and cynomolgus monkey FcRn by approximately 10-fold at pH 6.0 compared with huKID24, but retained weak/no binding at pH 7.0 (Fig. 1D). Second, cysteine residues were substituted at position 442 of the mAb heavy chains to facilitate site-specific CYSMAB conjugation (28).

MGA021 was conjugated to the next generation maytansinoid linker payload DM21-C to yield the IMGC936 ADC with a target DAR of approximately 2.0 (DAR range of 1.5–2.2; Fig. 2). The DM21-C linker payload incorporates a highly stable tripeptide linker (*L*-Ala-D-Ala-L-Ala) and a hydrophobic sulfur-bearing maytansinoid, which

has improved plasma stability, bystander killing activity, and a greater therapeutic window in mouse models than previously described maytansinoid conjugates (29).

### Expression of ADAM9 in Cancer and Normal Tissue

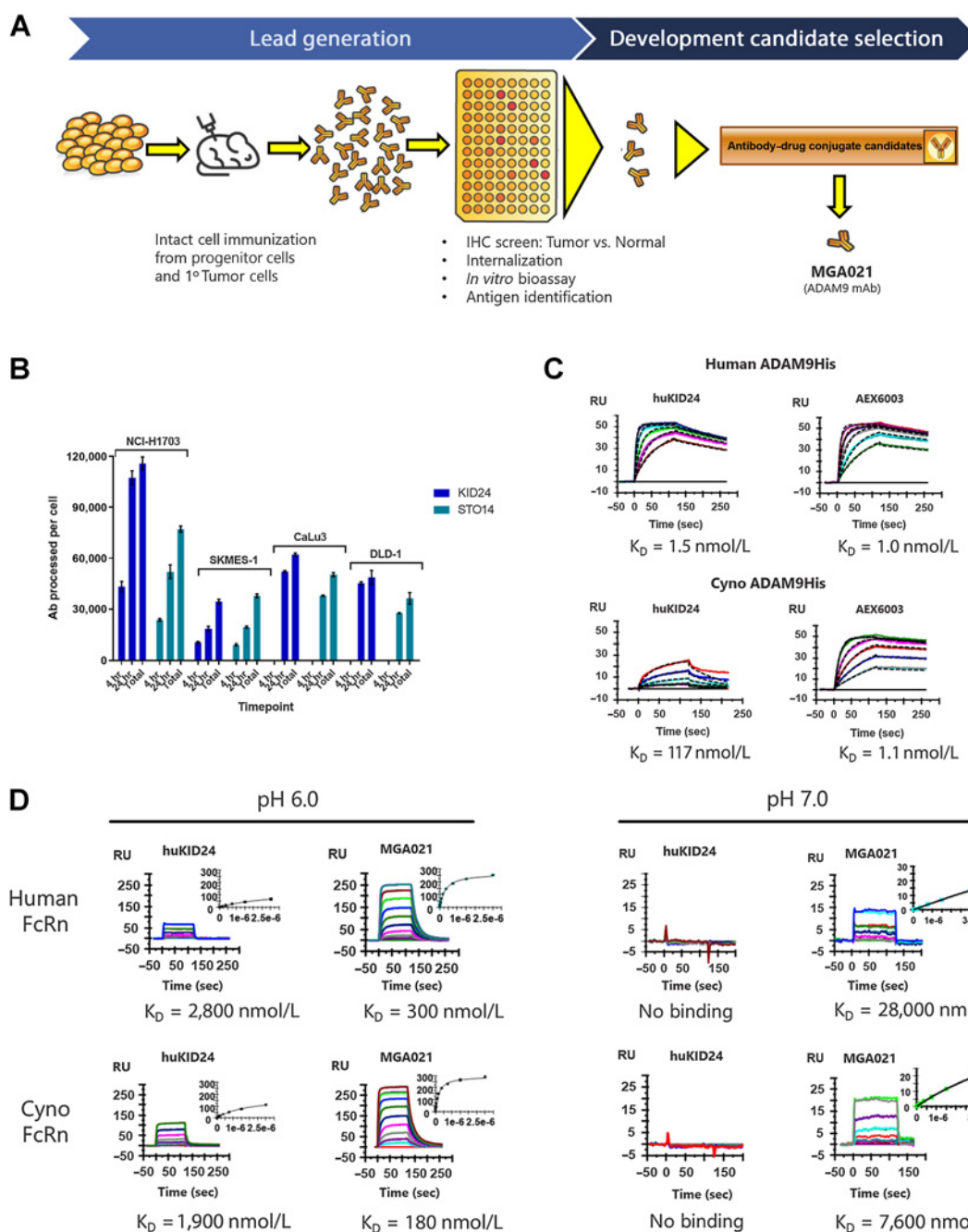
ADAM9 expression was evaluated by IHC in human tumor sections from various cancers, and consistent with published reports, high ADAM9 expression was observed across a range of cancers (Fig. 3). The majority of cancers examined showed ADAM9 positivity, and in the case of pancreatic cancer, gastric cancer, NSCLC adenocarcinoma, and triple-negative breast cancer (TNBC), greater than 60% of the tumor specimens in each indication exhibited H-scores greater than 100, and 10% to 30% exhibited H-scores greater than 200.

Conversely, ADAM9 expression was limited in normal tissues. In a good laboratory practice human tissue cross-reactivity study with IMGC936, limited frequency and intensity of membrane and cytoplasmic staining was observed in various epithelial cell types in bladder, cervix, esophagus, fallopian tube, kidney, large intestine, lung, mammary gland, ovary, pancreas, prostate, salivary gland, tonsil, ureter, and uterus. In addition, IMGC936 stained the membrane and cytoplasm of mononuclear cells in various tissues, including lymphoid tissues. Other membrane and cytoplasm staining noted included hematopoietic precursor cells in bone marrow, placenta trophoblasts, and neuropil. Of note, the majority of IMGC936 staining of epithelium was cytoplasmic in nature with distinct membrane staining only observed in rare epithelial cells at a 1–2+ level of intensity. Staining observed in membrane and cytoplasmic compartments was generally comparable between the human and cynomolgus monkey tissues and supports the cynomolgus monkey as an appropriate model for toxicity studies with IMGC936.

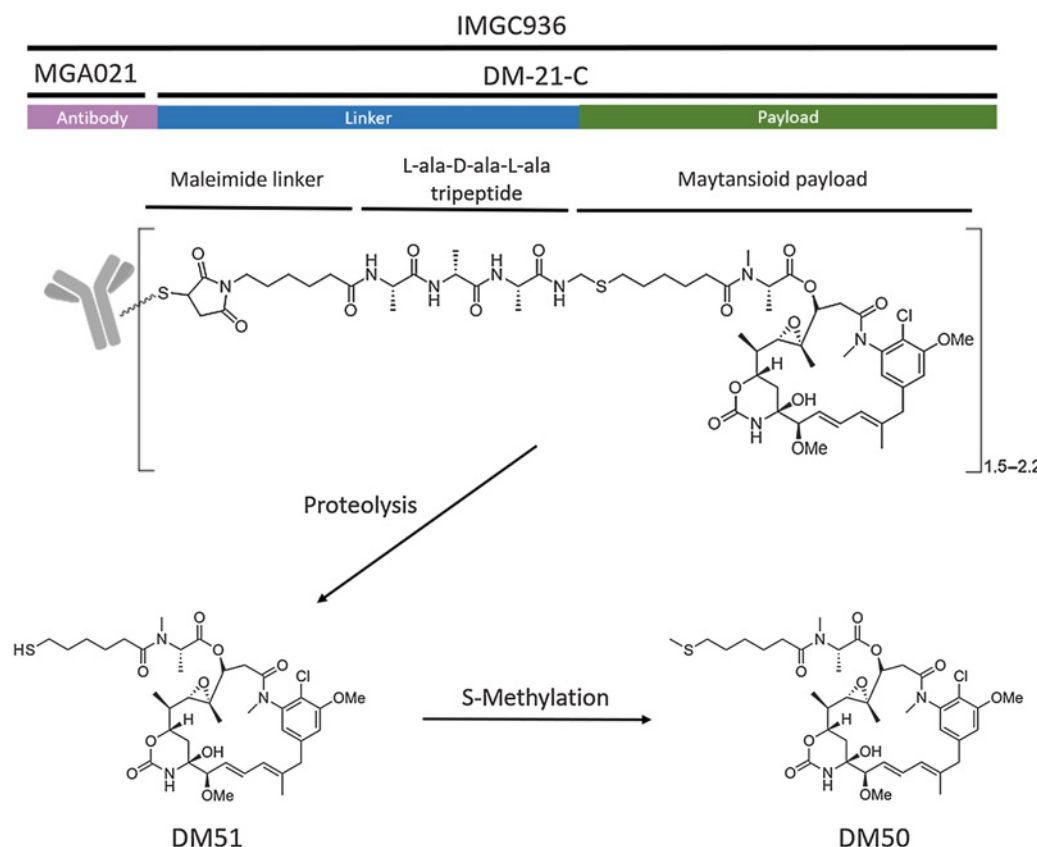
### *In vitro* profile of IMGC936

The cytotoxic potency of IMGC936 was evaluated *in vitro* against a panel of human tumor cell lines, originating from multiple cancer types, and expressing varying levels of ADAM9. The ADAM9 antigen density [antibody binding capacity (ABC)] on the cell lines ranged from 5,000 to 90,000. To evaluate the ADAM9-dependent potency of IMGC936, activity of hukTI-DM21-C, a control non-targeting DM21-C-bearing ADC against Kunitz soybean trypsin inhibitor that does not bind to either ADAM9 or any other human and murine protein, was also tested. The cytotoxicity of IMGC936 and the control ADC against representative human tumor cell lines is shown in Fig. 4A, and a summary of cytotoxicity results for all cell lines tested is shown in Supplementary Table S4. IMGC936 was cytotoxic toward all human tumor cell lines tested, with IC<sub>50</sub> values ranging from 0.2 to 224 nmol/L. The sensitivity of human tumor cell lines to IMGC936 was not strictly correlated with ADAM9 expression, indicating that other factors, such as rates of internalization and intracellular processing, may contribute to the overall sensitivity to IMGC936.

Due to the nature of the cleavable DM21-C linker-payload, the internalization and proteolytic processing of IMGC936 leads to the release of active metabolites (DM50/DM51) from tumor cells (Fig. 2). The released active metabolites have the potential to be internalized by neighboring tumor cells, irrespective of ADAM9 target expression, and mediate bystander killing (32). To assess bystander killing potential, a co-culture experiment was conducted in which RFP-expressing NCI-H1975 cells knocked out for ADAM9 (NCI-H1975/ADAM9 KO/RFP), were cultured alone, or in the presence of progressively larger numbers of unlabeled ADAM9-expressing parental NCI-H1975 cells. The cultures were incubated with IMGC936 and the number of

**Figure 1.**

**A**, Schematic of antibody discovery platform and ADC development candidate selection. **B**, Internalization and processing of anti-ADAM9 mAbs *in vitro*. Human tumor cell lines (NCI-H1703, SKMES-1, CaLu3, DLD-1) were treated with [<sup>3</sup>H]-labeled mAbs at sufficient concentrations to saturate cell surface ADAM9. Following washing to remove unbound mAb, cells were incubated for the indicated times then analyzed for antibody degradation as previously described (31). Shown in the graph is the amount of processed anti-ADAM9 mAb (KID24 or STO14) per cell for the indicated cell lines. **C**, SPR analysis of the binding of human (top) and cynomolgus monkey (bottom) ADAM9 proteins to captured huKID24 and AEX6003 (affinity matured huKID24). The black dashed lines represent the global fit to a 1:1 Langmuir model of binding curves obtained at ADAM9 concentrations of 0 (black), 6.25 (green), 12.5 (cyan), 25 (blue), 50 (red), or 100 (magenta) nmol/L. Dissociation constants ( $K_D$ ) are shown below the individual graphs. **D**, SPR analysis of the binding of human (top) and cynomolgus monkey (bottom) FcRn proteins to immobilized huKID24 and MGA021 at pH 6.0 (left) or pH 7.0 (right). The inserts represent the steady state affinity fit of colored binding curves showed on the graphs in successive order from the bottom to the top at FcRn concentrations of 0, 11.7, 23.4, 46.9, 93.8, 187.5, 375, 750, 1,500, and 3,000 nmol/L. Dissociation constants ( $K_D$ ) are shown below the individual graphs.

**Figure 2.**

Schematic representation of IMGC936 and DM21-C-Cys and the proteolytic release of the active metabolites DM51 and DM50. IMGC936 is comprised of the maytansinoid DM21-C conjugated to the MGA021 antibody. MGA021 is a humanized IgG1/kappa mAb composed of 2 IgG1 heavy chains of 452 amino acids and 2 kappa light chains of 218 amino acids. In IMGC936, each antibody molecule is conjugated to approximately 2.0 molecules of DM21-C [drug to antibody ratio (DAR) approximately 2.0] via site-specific conjugation to engineered cysteine residues at position 442 of the heavy chains. Following receptor-mediated internalization of IMGC936 the linker-payload DM21-C-Cys is released by proteases. Subsequently, further proteolysis of DM21-C-Cys releases DM51, which can undergo S-methylation to the related catabolite DM50 (32). DM51 and DM50 can then bind to intracellular tubulin and suppress microtubule dynamics resulting in microtubule depolymerization. DM51 and DM50 can also be released from dying cells and mediate bystander killing.

viable ADAM9-negative, RFP-labeled cells (only NCI-H1975/ADAM9 KO/RFP cells were visible) were monitored by time-lapse fluorescent microscopy over a period of 5 days. As shown in Fig. 4B, treatment with IMGC936 had no effect on the viability of NCI-H1975/ADAM9 KO/RFP cells when cultured alone (dark gray bar). Conversely, parental NCI-H1975 cells were sensitive to IMGC936 treatment (Fig. 4A). However, in the co-culture setting, bystander killing of NCI-H1975/ADAM9 KO/RFP cells was observed, and the magnitude of bystander killing increased as the number of parental NCI-H1975 cells increased (orange bars).

Consistent with the mechanism of action of tubulin-interacting maytansinoid compounds (33), treatment with IMGC936 led to arrest of NCI-H1703 tumor cells in the G<sub>2</sub>-M phase of the cell cycle (Fig. 4C). At 24 hours following treatment with 10 nmol/L IMGC936, the percentage of cells in the G<sub>2</sub>-M phase increased from 19.2% to 74.4%, with concomitant decreases in the percentage of cells in the G<sub>0</sub>-G<sub>1</sub> and S phases, indicative of cell-cycle arrest in the G<sub>2</sub>-M phase. Treatment with MGA021 (unconjugated IMGC936), or the non-targeting control ADC huKTI-DM21-C, had no impact on cell-cycle arrest.

Apoptosis was also assessed following treatment of tumor cells with IMGC936 for 48 hours. Overall, 49.1% of cells underwent apoptosis

(early apoptosis + late apoptosis) following 10 nmol/L IMGC936 treatment, with 41.4% early apoptotic and 7.7% late apoptotic at 48 hours (Fig. 4D). Treatment with MGA021 or the huKTI-DM21-C conjugate did not lead to apoptosis.

#### ***In vivo* antitumor activity of IMGC936**

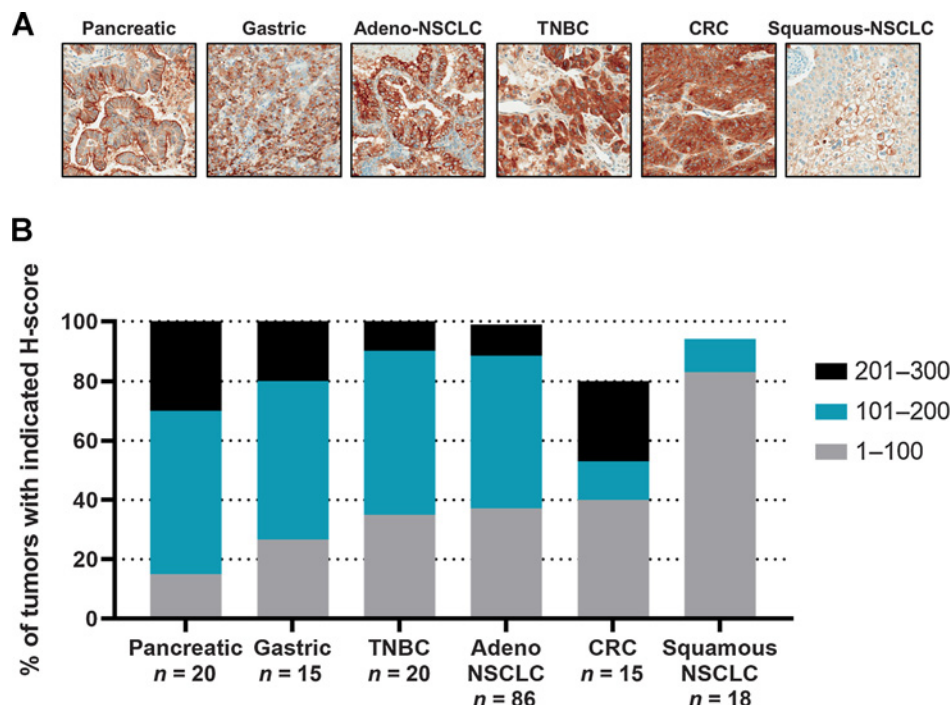
##### **CDX models**

Based on the encouraging *in vitro* cytotoxicity activity of IMGC936, we next assessed whether the *in vitro* activity translated to potent antitumor activity *in vivo*. Evaluation of *in vivo* antitumor activity of IMGC936 was conducted across a set of ADAM9-expressing human tumor CDX to (i) identify tumor types that exhibit sensitivity to IMGC936 and establish dose response profiles for IMGC936 following single-dose administration, (ii) confirm the requirement for targeted delivery of the active DM50/51 metabolites of IMGC936 to the tumor xenografts to achieve antitumor activity, and (iii) confirm the selectivity of IMGC936 to target ADAM9-expressing tumor xenografts.

IMGC936 exhibited broad, dose-dependent antitumor activity across models representing different tumor types and levels of ADAM9 expression (Fig. 5). A single-dose administration of 10 mg/kg IMGC936 led to a 90% or greater reduction in tumor

**Figure 3.**

ADAM9 Expression across a range of human cancers. **A**, representative images of ADAM9 staining of human FFPE tumor sections. **B**, summary of the semiquantitative IHC H-scores for the indicated cancers. Shown is the percent of tumors with H-scores ranging from 1–100 (gray), 101–200 (teal) and 201–300 (black) for each indication. H-score (range 0–300) is calculated according to the following formula:  $[1 \times (\% \text{ tumor cell (membrane + cytoplasm)} \text{ at } 1+) + 2 \times (\% \text{ tumor cell (membrane + cytoplasm)} \text{ at } 2+) + 3 \times (\% \text{ tumor cell (membrane + cytoplasm)} \text{ at } 3+)]$ .



volume compared with the vehicle control in all the models tested. Antitumor activity was also observed at the lower administered dose levels of IMGC936 in all ADAM9-positive models, including the lowest dose tested (2.5 or 1.25 mg/kg depending on the model).

Particularly deep and durable antitumor responses were noted for several of the models. Treatment of EBC-1 NSCLC xenografts with IMGC936 led to near complete reduction in tumor volume at all four dose levels tested, with the 10 and 5 mg/kg groups exhibiting durable complete regressions that were maintained until the end of the study (Fig. 5F). HPAF-II pancreatic adenocarcinoma xenografts exhibited a 92% reduction in tumor volume following IMGC936 treatment at 10 mg/kg compared with the vehicle control, while treatment at 5 mg/kg and 2.5 mg/kg resulted in an 86% and 70% reduction in tumor volume, respectively (Fig. 5A). IMGC936 induced complete regressions in 6/7 and 5/7 animals at doses of 10 and 5 mg/kg, respectively, in the HPAF-II study. SW48 colorectal carcinoma adenocarcinoma xenografts were also responsive to all three dose levels of IMGC936 tested (Fig. 5D). Treatment with IMGC936 at 10 mg/kg led to a 100% reduction in tumor volume (7/7 complete regressions) compared with the vehicle control, while treatment at 5 mg/kg and 2.5 mg/kg resulted in a 97% (3/7 complete regressions) and 59% reduction in tumor volume, respectively. Of the six models described in this report, SW48 was the only model where partial activity from the nontargeting control ADC was observed. We hypothesize this may be due to sensitivity of the model to maytansinoid-mediated cytotoxicity *in vivo*, and/or active macropinocytosis in this model (34).

To confirm the requirement for targeted delivery of payload to the tumor xenograft to achieve antitumor activity, the sensitivity of EBC-1 NSCLC squamous xenografts to MGA021 alone, DM50 alone or the combination of MGA021 plus DM50 was compared with IMGC936. The DM50 concentration used was equivalent that present

in IMGC936 in the study. As shown in Fig. 5F, in contrast to IMGC936, neither MGA021, DM50, nor MGA021 plus DM50 were active toward the IMGC936-sensitive EBC-1 xenografts.

Finally, to confirm targeting specificity, the antitumor activity of IMGC936 was assessed in EBC-1 NSCLC squamous xenografts that lacked ADAM9 expression (ADAM9 gene knocked out). As shown in Fig. 5G, treatment with IMGC936 resulted in only a minimal decrease in tumor volume, equivalent to the control ADC, when compared with the vehicle control. Individual animal tumor volume data for all models is shown in Supplementary Fig. S4.

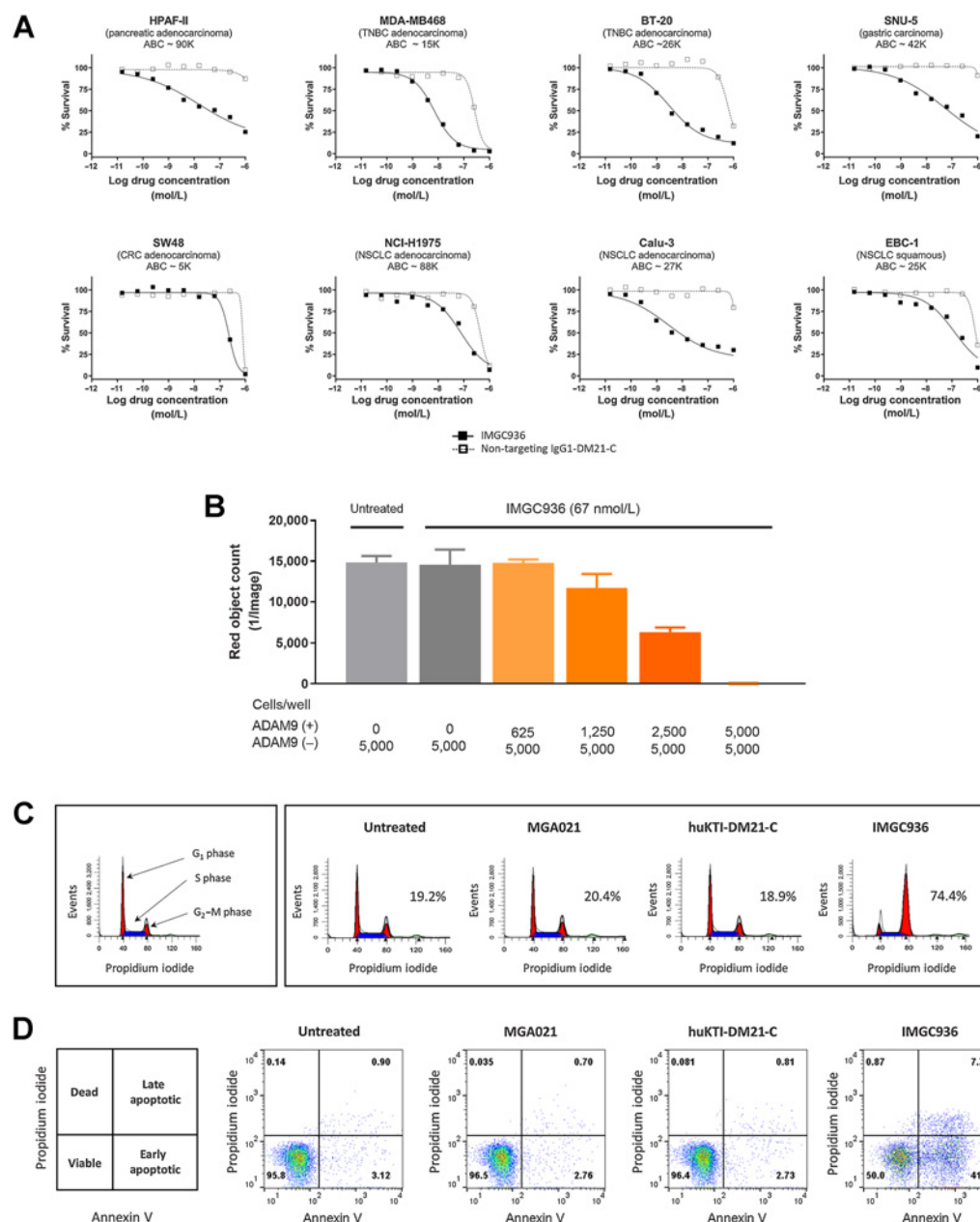
#### PDX models

The antitumor activity of a single-dose administration of IMGC936 at 8.6 mg/kg was also evaluated in heterogeneous ADAM9 expressing PDX models representing TNBC, NSCLC, pancreatic, and gastric cancer. Treatment of a TNBC PDX model (H-score 202) with IMGC936 led to rapid tumor regression and complete elimination of the tumors (Fig. 6A). In a pancreatic cancer PDX model (H-score 185), treatment with IMGC936 caused tumor stasis, with an overall reduction in tumor volume of 87% compared with the vehicle control (Fig. 6B). Similarly, in a gastric cancer PDX model (H-score 127), IMGC936 treatment resulted in tumor stasis, with an overall reduction in tumor volume of 87% compared with the vehicle control (Fig. 6C). Finally, in a NSCLC PDX model (H-score 186), treatment with IMGC936 caused rapid tumor regression and complete elimination of the tumors (Fig. 6D). A detailed summary of ADAM9 H-scores for the PDX models is shown in Supplementary Tables S5.

IMGC936 was well tolerated in all mouse models tested. No significant weight loss or clinical signs of toxicity were observed.

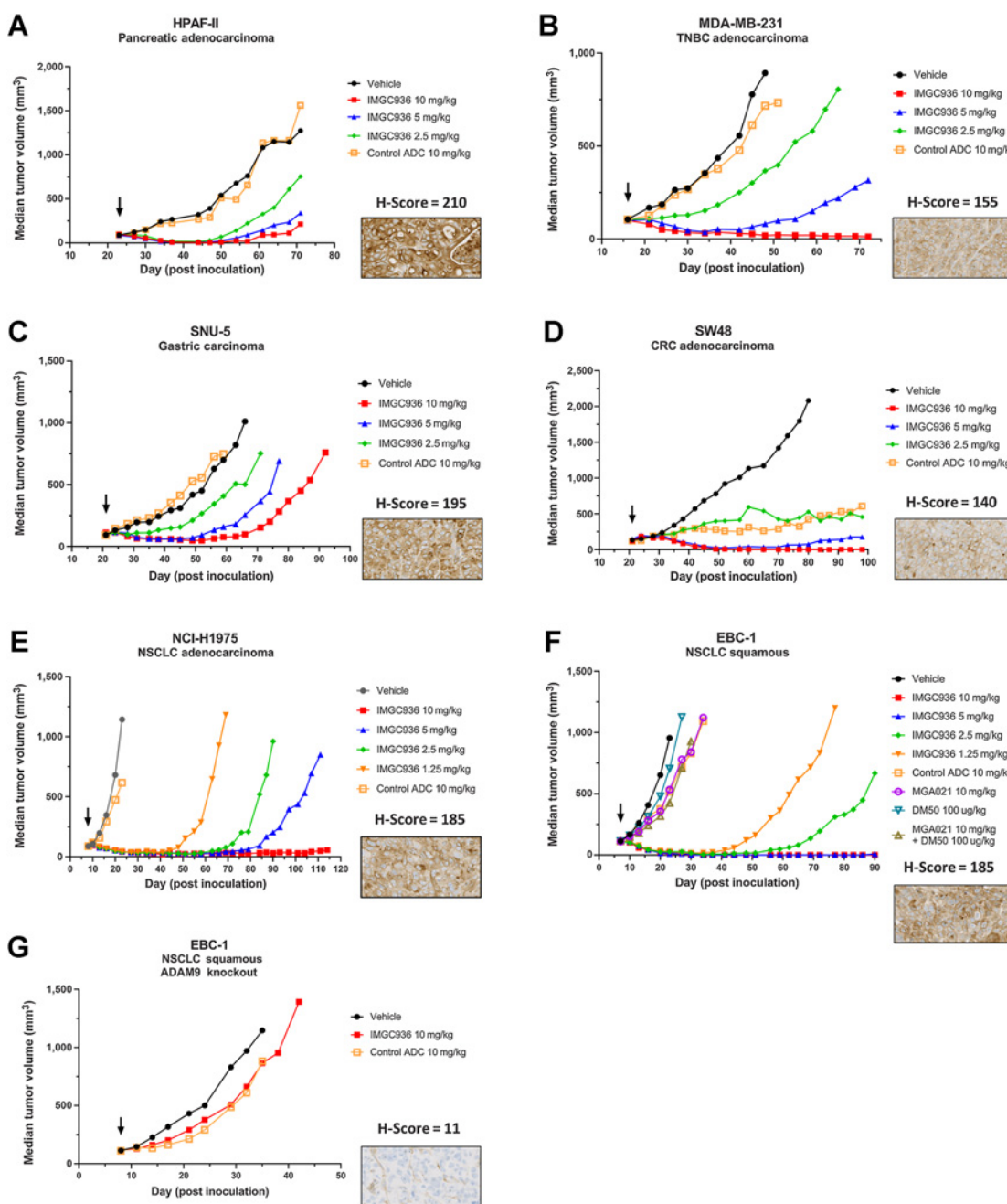
#### Tolerability and toxicokinetics of IMGC936

IMGC936 was administered at a two-week interval (total of 2 doses) at dose levels of 0, 3, 10, and 22.5 mg/kg/dose in cynomolgus monkeys.



**Figure 4.**

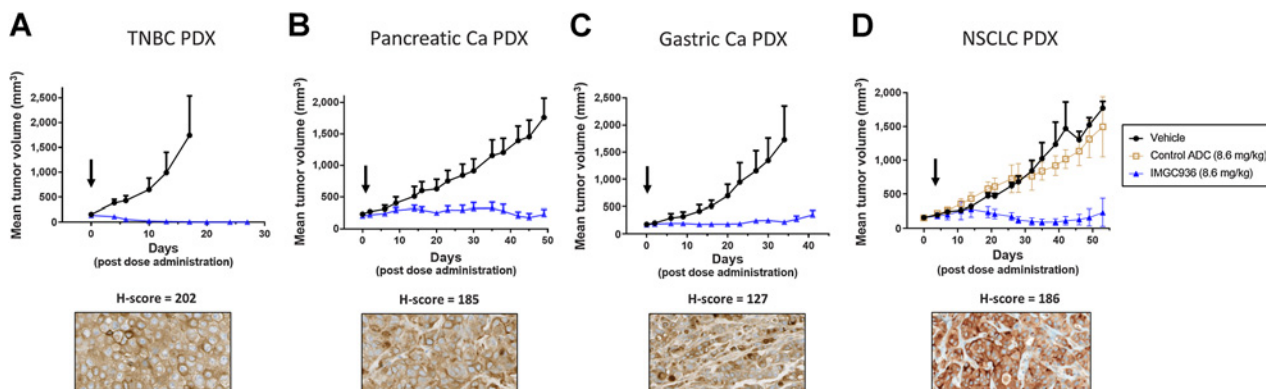
**A**, Evaluation of IMGC936 *in vitro* cytotoxicity toward ADAM9-positive human tumor cell lines. IMGC936 (solid squares) was compared with the non-targeting IgG1-DM21-C control ADC (huKTI-DM21-C; open squares). Cell cytotoxicity was measured by the WST-8 cytotoxicity assay. **B**, Evaluation of bystander killing by IMGC936. 5,000 NCI-H1975 cells in which ADAM9 had been stably knocked out (NCI-H1975/ADAM9 KO/RFP cells expressing red fluorescent protein; ADAM9-negative) were cultured alone, or with the indicated number of parental NCI-H1975 cells (unlabeled; ADAM9-positive). Cultures were treated with 67 nmol/L IMGC936 or left untreated. The number of red fluorescent NCI-H1975/ADAM9 KO/RFP cells remaining following the 5-day incubation were counted with an IncuCyte Live-Cell Analysis System. **C**, Cell-cycle analysis of NCI-H1703 cells treated with 10 nmol/L IMGC936, MGA021 and huKTI-DM21-C control for 24 hours. Propidium iodide is a fluorescent nuclear stain that cannot pass through undamaged membranes of human cells. Ethanol treatment permeabilizes the cell membrane and allows this dye to enter the cells and bind to DNA. The amount of propidium iodide bound is directly proportional to the amount of DNA in the cell and can be used to distinguish the G<sub>0</sub>-G<sub>1</sub>, S, and G<sub>2</sub>-M phases of the cell cycle. The propidium iodide in each cell was quantitated by flow cytometry. The number shown in each panel represents the percentage of the total cell population in G<sub>2</sub>-M phase. **D**, Analysis of apoptosis by flow cytometry: annexin V and propidium iodide staining of NCI-H1703 cells treated with 10 nmol/L IMGC936, MGA021 and huKTI-DM21-C control for 48 hours. Both Annexin V and propidium iodide are membrane impermeable stains. Annexin V binds to phosphatidylserine, which translocates to the outer surface of the cell membrane during the earliest stages of apoptosis. Propidium iodide binds to DNA of cells with damaged plasma membranes, thus its signal is indicative of dead cells in the population. Using this dual staining method, one can discern dead cells from the cells that are in the early stages of apoptosis, yet still have an intact membrane. As such, early apoptosis is defined as annexin V-positive/propidium iodide-negative, while late apoptosis is defined as annexin V-positive/propidium iodide-positive. The number shown in each quadrant represents the percentage of the total cell population in the respective quadrant.

**Figure 5.**

Antitumor activity of IMGC936 across multiple CDX models. Mice bearing human tumor xenografts were administered a single-dose of IMGC936, MGA021, DM50, MGA021 plus DM50 or the control ADC (huTKT1-DM21-C) at the indicated concentrations. **A**, HPAF-II pancreatic adenocarcinoma xenografts. **B**, MDA-MB-231 TNBC adenocarcinoma xenografts. **C**, SNU-5 gastric carcinoma xenografts. **D**, SW48 colorectal adenocarcinoma xenografts. **E**, NCI-H1975 NSCLC adenocarcinoma xenografts. **F**, EBC-1 NSCLC squamous xenografts. **G**, EBC-1 NSCLC squamous xenografts, in which ADAM9 was knocked out. Arrows indicate the day of dose administration.

There were no differences noted between control animals and animals that received IMGC936 (up to 22.5 mg/kg/dose) in body weights, food consumption, physical examinations, body temperature, electrocardiography, blood pressure, visual respiratory rate, clinical pathology parameters (hematology, coagulation, and clinical chemistry), gross necropsy or organ weights.

No IMGC936-related clinical observations were noted at 3 mg/kg/dose. All other IMGC936-related study observations were dose dependent and occurred with greater frequency and earlier time points at 22.5 mg/kg/dose as compared with 10 mg/kg/dose. Clinical observations were limited to skin changes (dry, red and/or black hyperpigmentation). Ophthalmic examinations which included slit lamp

**Figure 6.**

ADAM9 expression and antitumor activity of IMGC936 in PDX models. Each subpanel shows representative images and H-scores of FFPE staining for ADAM9 and tumor growth in mice treated with a single-dose administration of IMGC936 or the control ADC (huTKT1-DM21-C) at 8.6 mg/kg. **A**, TNBC. **B**, Pancreatic adenocarcinoma. **C**, Gastric adenocarcinoma. **D**, NSCLC adenocarcinoma. Arrows indicate the day of dose administration.

biomicroscopy and indirect ophthalmoscopy, revealed corneal pigmentation at  $\geq 10$  mg/kg/dose and included corneal cloudiness, cellular/keratic precipitates, and pannus at the 22.5 mg/kg/dose level. Terminal euthanasia microscopic findings at 10 mg/kg/dose consisted of minimal single cell necrosis of corneal epithelial cells that increased in severity to minimal to moderate and included minimal increased mitoses in the cornea at 22.5 mg/kg/dose. Decreased thymus lymphoid cellularity was noted as minimal, or mild to moderate, in animals that received 10 or 22.5 mg/kg/dose, respectively. After the 6-week recovery period, the thymus finding had resolved, while the eye (cornea) microscopic findings were still observed, but at lower levels of severity, indicating ongoing resolution.

A single male (22.5 mg/kg/dose) was found dead on day 34, 19 days following the last dose administration. The majority of the findings (clinical observations and microscopic findings) were similar or increased compared with those observed in other study animals and also included body weight loss of 12.5% (days 21–28), changes in clinical pathology parameters (without microscopic correlates) due to subclinical dehydration, and moderate degeneration/necrosis of the urinary bladder transitional epithelium together with infiltration of mixed inflammatory cells. Although the cause of death was not apparent, a relationship to IMGC936 administration could not be ruled out.

The toxicokinetic profile of IMGC936 was obtained in cynomolgus monkeys receiving 3, 10, or 22.5 mg/kg/dose administered on days 1 and 15. As shown in Supplementary Fig. S5, IMGC936 exhibited favorable stability in the cynomolgus monkey, with the conjugated and total mAb concentration versus time curves superimposed upon each other, and minimal release of DM50/51 metabolites. Consistent with the stability of IMGC936 in cynomolgus serum,  $C_{max}$ , exposure and clearance of conjugated and total antibody were similar within each dose level, and the detectable amount of unconjugated DM50/51 was very low. After the first dose, the mean CL value at 3 mg/kg/dose was 3.6- and 5.8-fold higher (conjugated mAb) and 3.4- and 4.9-fold higher (total mAb) than CL values at 10 and 22.5 mg/kg/dose, respectively. After the second dose, the disparity in CL at 3 mg/kg/dose compared with the higher doses was greater and exposure parameters ( $C_{max}$  and AUC) increased more than proportional to the increase in dose from 3 to 10 mg/kg/dose. The more-than-proportional increases in exposure and the decrease in CL of both conjugated and total antibody with

increasing dose of IMGC936 are consistent with nonlinear pharmacokinetics, and may be due to target-mediated drug disposition (TMDD) at the lower dose, saturation of target specific clearance mechanisms with increasing doses, and in the case of the second dose, formation of anti-drug antibodies (ADA), that are not apparent at the higher doses. While systemic exposure did not change following repeated biweekly IV infusion of IMGC936, exposure decreased in a few animals that received 3 mg/kg/dose during the second dose interval due to the development of ADA. IMGC936, administered at a 2-week interval, had observed accumulation after repeat dosing at 10 and 22.5 mg/kg/dose. The 10 mg/kg/dose, the highest nonseverely toxic dose level, corresponded to a peak and systemic exposure of 222  $\mu$ g/mL ( $C_{max}$ ) and 23,400  $hr \cdot \mu$ g/mL (AUC<sub>0-336</sub>) for the conjugated antibody, 233  $\mu$ g/mL ( $C_{max}$ ) and 24,400  $hr \cdot \mu$ g/mL (AUC<sub>0-336hr</sub>) for the total antibody, 0.83 ng/mL ( $C_{max}$ ) and 23.6  $hr \cdot ng/mL$  (AUC<sub>0-336hr</sub>) for DM51, and 0.013 ng/mL ( $C_{max}$ ) for DM50. Associated accumulation levels were 1.69 and 1.40 for conjugated and antibody total antibody, respectively. The pharmacokinetic parameters, derived from non-compartmental analysis for conjugated antibody, total antibody, DM51, and DM50 are summarized in Supplementary Tables S6-S9.

## Discussion

In this article we describe the preclinical profile of IMGC936, a next generation maytansinoid-based ADC targeting ADAM9 that incorporates half-life extension and site-specific CYSMAB conjugation technologies. ADAM9 expression was observed in a diverse set of solid tumors with significant unmet clinical need. While cell surface proteases have attracted some interest in the past as targets for small molecule enzyme inhibitors, our current approach relies only on the expression of ADAM9 to exert pharmacologic effect. IMGC936-mediated potent cytotoxicity toward ADAM9-expressing tumor cell lines representing a range of cancer types – with evidence of cells arresting at the G<sub>2</sub>–M phase of the cell cycle and displaying markers of apoptosis. Consistent with a previous report (29), the DM21-C linker-payload incorporated into IMGC936 induced bystander killing of ADAM9-negative tumor cells when cultured in the presence of ADAM9-positive tumor cells. IMGC936 exhibited antitumor activity toward NSCLC, gastric, pancreatic, TNBC, and colorectal cancer CDX models following a single-dose administration at dose levels predicted

to be achievable in the clinic based on the safety profile in the cynomolgus monkey. The antitumor activity of IMGC936 was also observed in TNBC, NSCLC, gastric, and pancreatic cancer PDX models with heterogeneous expression of ADAM9. A single-dose administration of IMGC936 at 8.6 mg/kg resulted in complete responses in 3/3 mice for the TNBC (H-score 202) and NSCLC (H-score 186) PDX models, consistent with the bystander killing observed *in vitro*, highlighting the potential for IMGC936 to eradicate heterogeneous ADAM9 expressing tumors.

In the cynomolgus monkey, IMGC936 was tolerated at 10 mg/kg/dose when administered once every two weeks (total of 2 doses), with a toxicology profile generally consistent with the platform toxicity profile associated with maytansines (35, 36). IMGC936-related reversible ocular effects were anticipated in the cynomolgus monkey, despite the lack of IMGC936 reactivity in the eye, based on the known ocular toxicity of the maytansinoid payload (37–40) which can be mitigated or minimized in the clinic. Ocular events associated with the first-in-human studies with mirvetuximab soravtansine, a maytansinoid DM4-based ADC targeting folate receptor alpha, were successfully managed in subsequent clinical trials by employing adjusted ideal body weight to calculate dose (41) and implementation of prophylactic lubricating and steroid eye drops (42, 43).

A major challenge encountered with ADCs is delivery of sufficient amounts of payload to the intracellular target of the tumor. The ability of an ADC to deliver payload is influenced by many factors – the ADC must be stable in systemic circulation, reach the tumor, bind to its specific cell surface antigen, internalize, and release the payload at the site of action. To maximize delivery to tumors, several innovations have been incorporated into IMGC936. These innovations include the next generation DM21-C linker-payload, with its highly stable tripeptide linker ( $\text{l-Ala-D-Ala-L-Ala}$ ), which exhibits greater plasma stability than previous sulfo-SPDB-DM4 linker-payloads (44). In addition, the highly potent, cell permeable sulfur-bearing maytansinoids (DM50 and DM51), exhibit enhanced bystander killing activity (29). Although the low normal tissue expression of ADAM9 suggested TMDD would have minimal impact on the pharmacokinetic properties of IMGC936, TMDD has been shown to contribute to reduced half-life and low exposure of many therapeutic mAbs, especially at low dose levels (45). To maximize the half-life and exposure of IMGC936, the YTE triple mutation was engineered into the Fc domain to improve binding to the neonatal Fc receptor at low pH, increase recycling of FcRn bound IMGC936, thus increasing serum half-life (46). Several studies have shown that ADCs with a lower DAR can have improved tumor penetration and larger therapeutic windows than ADCs with a higher DAR, when dosed at equivalent payload concentrations (47–49). This is hypothesized to be a function of improved pharmacokinetic properties of the ADC (increased exposure and reduced clearance at lower DAR (48), and protein concentration-driven penetration of the ADCs into the tumor (50). To take advantage of these observations, cysteine conjugation sites were engineered into the Fc domain (HC-C442) of IMGC936 to facilitate site-specific conjugation at an average DAR of approximately 2.0, which may enable administration of higher dose levels of IMGC936, while also providing for a more homogenous ADC distribution in the tumor.

Of note, IMGC936 is not cross-reactive with mouse ADAM9, so potential effects of target-mediated drug distribution would not be modeled in the mouse xenograft studies. Therefore, preclinical evaluations of a therapeutic window based on tolerability and antitumor

response is more appropriately made using drug exposure parameters rather than administered dose levels. The systemic exposure of conjugated mAb in the cynomolgus monkey at 10 mg/kg/dose was 23,400 hr· $\mu\text{g}/\text{mL}$  following the first dose, while the exposure in CD-1 nude mice was 1995 hr· $\mu\text{g}/\text{mL}$  after a single 5 mg/kg dose (Supplementary Table S10). In the single-dose administration dose ranging CDX studies, IMGC936 was highly active at 1.25 mg/kg in two models, and at 5 mg/kg in two other models. With the recognition that repeat-dose administration of ADCs is standard in the clinic to achieve therapeutic benefit, a comparison of the exposure of IMGC936 following repeat-dose administration in cynomolgus monkey to that in mouse preclinical models following a single-dose administration, provides evidence of a large therapeutic index for IMGC936, and a potentially favorable clinical therapeutic window.

In conclusion, we have developed an anti-ADAM9 ADC, IMGC936, that incorporates three innovations—a next generation maytansine-based linker-payload with increased stability and improved bystander killing, half-life extension through incorporation of the YTE triple mutation in the Fc domain, and engineered cysteine residues to facilitate DAR 2 site-specific conjugation. IMGC936 exhibited cytotoxicity toward ADAM9-positive human tumor cell lines, as well as bystander killing, potent antitumor activity in preclinical CDX and PDX tumor models, and a favorable pharmacokinetic and acceptable safety profile in cynomolgus monkeys. The preclinical data supports the continued development of IMGC936 for the treatment of ADAM9-positive solid tumors. A first-in-human study of IMGC936 in patients with advanced solid tumors has been initiated (NCT04622774).

## Authors' Disclosures

J.A. Scribner reports a patent for WO2018119196 pending, a patent for WO2020005945 pending, and a patent for PCT/US2022/019133 pending. S.W. Hicks reports a patent for 17/255,064 pending. K.W. Sinkevicius reports I was an employee of ImmunoGen during this study and then a paid consultant of MacroGenics for several months. G. Diedrich reports a patent for WO2018119196 pending and a patent for WO2020005945 pending. F.Z. Chen reports a patent for PCT/US2022/019133 pending. B. Barat reports a patent for WO2018119196 pending and a patent for WO2020005945 pending. K.A. McEachem reports other support from ImmunoGen during the conduct of the study. E.H. Westin reports other support from ImmunoGen during the conduct of the study; and Employee ImmunoGen. E. Bonvini reports a patent for WO2018119196 pending and a patent for WO2020005945 pending. D. Loo reports patent for WO2018119196 pending, patent for WO2020005945 pending, and a patent for PCT/US2022/019133 pending. No disclosures were reported by the other authors.

## Authors' Contributions

**J.A. Scribner:** Conceptualization, formal analysis, supervision, investigation, methodology, writing—original draft, writing—review and editing. **S.W. Hicks:** Conceptualization, formal analysis, supervision, methodology, writing—original draft, writing—review and editing. **K.W. Sinkevicius:** Conceptualization, formal analysis, supervision, investigation, methodology, writing—review and editing. **N.C. Yoder:** Conceptualization, formal analysis, supervision, investigation, methodology, writing—review and editing. **G. Diedrich:** Conceptualization, formal analysis, supervision, investigation, methodology, writing—review and editing. **J.G. Brown:** Conceptualization, formal analysis, supervision, methodology, writing—review and editing. **J. Lucas:** Conceptualization, formal analysis, supervision, investigation, methodology, writing—review and editing. **M.E. Fuller:** Conceptualization, formal analysis, supervision, investigation, methodology. **T. Son:** Investigation, methodology, writing—review and editing. **A. Dastur:** Investigation, methodology, writing—review and editing. **J. Hooley:** Investigation, methodology, writing—review and editing. **C. Espelin:** Conceptualization, formal analysis, supervision, investigation, methodology, writing—review and editing. **M. Themeles:** Conceptualization, formal analysis, supervision, investigation, methodology. **F.Z. Chen:** Conceptualization, supervision,

investigation, methodology. **Y. Li:** Conceptualization, supervision, investigation, methodology. **M. Chiechi:** Investigation, methodology. **J. Lee:** Investigation, methodology. **B. Barat:** Investigation, methodology. **L. Widjaja:** Investigation, methodology. **S. Gorlatov:** Investigation, methodology. **J. Tamura:** Supervision, investigation, methodology. **V. Ciccarone:** Supervision, investigation, methodology. **O. Ab:** Writing-review and editing. **K.A. McEachem:** Conceptualization, supervision, investigation, methodology. **S. Koenig:** Conceptualization, supervision, writing-review and editing. **E.H. Westin:** Conceptualization, supervision. **P.A. Moore:** Conceptualization, supervision, writing-review and editing. **T. Chittenden:** Conceptualization, supervision. **R.J. Gregory:** Conceptualization, supervision, writing-review and editing. **E. Bonvini:** Conceptualization, supervision, writing-review and editing. **D. Loo:**

Conceptualization, formal analysis, supervision, methodology, writing-original draft, writing-review and editing.

## Acknowledgments

The authors wish to thank Jennie Mather and Penny Roberts for their vision and leadership in the development of the innovative antibody/target discovery platform, Monica Licea and Tony Liang for their early contributions to the antibody/target discovery platform, and Alice Ku for project management.

Received November 23, 2021; revised March 3, 2022; accepted April 27, 2022; published first May 5, 2022.

## References

1. Oria VO, Lopatta P, Schilling O. The pleiotropic roles of ADAM9 in the biology of solid tumors. *Cell Mol Life Sci* 2018;75:2291–301.
2. Izumi Y. A metalloprotease-disintegrin, MDC9/meltrin-gamma/ADAM9 and PKCdelta are involved in TPA-induced ectodomain shedding of membrane-anchored heparin-binding EGF-like growth factor. *EMBO J* 1998;17:7260–72.
3. Karadag A, Zhou M, Croucher PI. ADAM9 (MDC-9/meltrin-gamma), a member of the a disintegrin and metalloproteinase family, regulates myeloma cell-induced interleukin-6 production in osteoblasts by direct interaction with the  $\alpha(v)\beta 5$  integrin. *Blood* 2006;107:3271–8.
4. Kohga K, Tatsumi T, Takehara T, Tsunematsu H, Shimizu S, Yamamoto M, et al. Expression of CD133 confers malignant potential by regulating metalloproteinases in human hepatocellular carcinoma. *J Hepatol* 2010;52:872–9.
5. Zigrino P, Nischt R, Mauch C. The disintegrin-like and cysteine-rich domains of ADAM9 mediate interactions between melanoma cells and fibroblasts. *J Biol Chem* 2011;286:6801–7.
6. Micocci KC, de Oliveira Moritz MN, Lino RLB, Fernandes LR, Lima AGF, Figueiredo CC, et al. ADAM9 silencing inhibits breast tumor cells transmigration through blood and lymphatic endothelial cells. *Biochimie* 2016;128:9:174–82.
7. Chiu K-L, Lin Y-S, Kuo T-T, Lo C-C, Huang Y-K, Chang H-F, et al. ADAM9 enhances CDCP1 by inhibiting miR-1 through EGFR signaling activation in lung cancer metastasis. *Oncotarget* 2017;8:47365–78.
8. O'shea C, McKiss N, Buggy Y, Duggan C, Hill ADK, Mcdermott E, et al. Expression of ADAM9 mRNA and protein in human breast cancer. *Int J Cancer* 2003;105:754–61.
9. Grützmann R, Lüttges J, Sipos B, Ammerpohl O, Dobrowski F, Alldinger I, et al. ADAM9 expression in pancreatic cancer is associated with tumor type and is a prognostic factor in ductal adenocarcinoma. *Br J Cancer* 2004;90:1053–8.
10. Oria VO, Lopatta P, Schmitz T, Preca BT, Nyström A, Conrad C, et al. ADAM9 contributes to vascular invasion in pancreatic ductal adenocarcinoma. *Mol Oncol* 2019;13:456–79.
11. Wang J, Zhou Y, Fei X, Chen X, Yan J, Liu B, et al. ADAM9 functions as a promoter of gastric cancer growth which is negatively and posttranscriptionally regulated by miR-126. *Oncol Rep* 2017;37:2033–40.
12. Zhang J, Qi J, Chen N, Fu W, Zhou B, He A. High expression of a disintegrin and metalloproteinase-9 predicts a shortened survival time in completely resected stage I non-small cell lung cancer. *Oncol Lett* 2013;5:1461–6.
13. Kossmann CM, Annereau M, Thomas-Schoemann A, Nicco-Overney C, Chéreau C, Batteux F, et al. ADAM9 expression promotes an aggressive lung adenocarcinoma phenotype. *Tumour Biol* 2017;39:1010428317716077.
14. Fritzsche FR, Wassermann K, Jung M, Tölle A, Kristiansen I, Lein M, et al. ADAM9 is highly expressed in renal cell cancer and is associated with tumor progression. *BMC Cancer* 2008;8:179.
15. Mohd Isa SA, Md Salleh MS, Ismail M, Mohd Hairon S. ADAM9 expression in uterine cervical cancer and its associated factors. *Asian Pac J Cancer Prev* 2019; 20:1081–7.
16. Fritzsche FR, Jung M, Tölle A, Wild P, Hartmann A, Wassermann K, et al. ADAM9 expression is a significant and independent prognostic marker of PSA relapse in prostate cancer. *Eur Urol* 2008;54:1097–106.
17. Tao K, Qian N, Tang Y, Ti Z, Song W, Cao D, et al. Increased expression of a disintegrin and metalloprotease-9 in hepatocellular carcinoma: implications for tumor progression and prognosis. *Jpn J Clin Oncol* 2010;40:645–51.
18. Xiang L-Y, Ou H-H, Liu X-C, Chen Z-J, Li X-H, Huang Y, et al. Loss of tumor suppressor miR-126 contributes to the development of hepatitis B virus-related hepatocellular carcinoma metastasis through the upregulation of ADAM9. *Tumour Biol* 2017;39:1010428317709128.
19. Fan X, Wang Y, Zhang C, Liu L, Yang S, Wang Y, et al. ADAM9 expression is associate with glioma tumor grade and histological type, and acts as a prognostic factor in lower-grade gliomas. *Int J Mol Sci* 2016;17:1276.
20. Ueno M, Shiomi T, Mochizuki S, Chijiwa M, Shimoda M, Kanai Y, et al. ADAM9 is over-expressed in human ovarian clear cell carcinomas and suppresses cisplatin-induced cell death. *Cancer Sci* 2018;109:471–82.
21. Tanasubsin P, Aung WPP, Pata S, Laopajon W, Makeudom A, Sastraruji T, et al. Overexpression of ADAM9 in oral squamous cell carcinoma. *Oncol Lett* 2018; 15:495–502.
22. Chari RVJ, Miller ML, Widdison WC. Antibody-drug conjugates: an emerging concept in cancer therapy. *Angew Chem Int Ed Engl* 2014;53:3796–827.
23. Polakis P. Antibody drug conjugates for cancer therapy. *Pharmacol Rev* 2016;68: 3–19.
24. Mather JP, Fieger C, Liang TW, King KL, Li J, Young P, et al. A stem cell-based platform for the discover and development of antitumor therapeutic antibodies to novel targets. *Recombinant Antibodies for Immunotherapy* 2009; 313–35. Cambridge University Press.
25. Loo D, Beltejar C, Hooley J, Xu X. Primary and multipassage culture of human fetal kidney epithelial progenitor cells. *Methods Cell Biol* 2008;86:241–55.
26. Douthwaite JA, Sridharan S, Huntington C, Hammersley J, Marwood R, Hakulinen JK, et al. Affinity maturation of a novel antagonistic human monoclonal antibody with a long VH CDR3 targeting the Class A GPCR formyl-peptide receptor 1. *MAbs* 2015;7:152–66.
27. Groves MA, Amanuel L, Campbell JI, Rees DG, Sridharan S, Finch DK, et al. Antibody VH and VL recombination using phage and ribosome display technologies reveals distinct structural routes to affinity improvements with VH-VL interface residues providing important structural diversity. *MAbs* 2014;6:236–45.
28. Bai C, Reid EE, Wilhelm A, Shizuka M, Maloney EK, Laleau R, et al. Site-specific conjugation of the indolinobenzodiazepine DGN549 to antibodies affords antibody-drug conjugates with an improved therapeutic index as compared with lysine conjugation. *Bioconjug Chem* 2020;31:93–103.
29. Costoplus JA, Veale KH, Qiu Q, Ponte JF, Lanieri L, Setiady Y, et al. Peptide-cleavable self-immolative maytansinoid antibody-drug conjugates designed to provide improved bystander killing. *ACS Med Chem Lett* 2019;10:1393–9.
30. Scribner JA, Barat B, Hicks SW, Yoder NC, Son T, Widjaja L, et al. *Cancer Res* 2017;77(13 Suppl):38.
31. Lai KC, Deckert J, Setiady YY, Shah P, Wang L, Chari R, et al. Evaluation of targets for maytansinoid ADC therapy using a novel radiochemical assay. *Pharm Res* 2015;32:3593–603.
32. Erickson HK, Park PU, Widdison WC, Kovtun YV, Garrett LM, Hoffman K, et al. Antibody-maytansinoid conjugates are activated in targeted cancer cells by lysosomal degradation and linker-dependent intracellular processing. *Cancer Res* 2006;66:4426–33.
33. Oroudjev E, Lopus M, Wilson L, Audette C, Provenzano C, Erickson H, et al. Maytansinoid-antibody conjugates induce mitotic arrest by suppressing microtubule dynamic instability. *Mol Cancer Ther* 2010;9:2700–13.
34. Ha KD, Bidlingmaier SM, Liu B. Macropinocytosis exploitation by cancers and cancer therapeutics. *Front Physiol* 2016;7:381.
35. Donaghy H. Effects of antibody, drug and linker on the preclinical and clinical toxicities of antibody-drug conjugates. *MAbs* 2016;8:659–71.
36. De Goeij BE, Lambert JM. New developments for antibody-drug conjugate-based therapeutic approaches. *Curr Opin Immunol* 2016;40:14–23.
37. Ab O, Whiteman KR, Bartle LM, Sun X, Singh R, Tavares D, et al. IMGN853, a folate receptor-alpha (FR $\alpha$ )-targeting antibody-drug conjugate, exhibits potent targeted antitumor activity against FR $\alpha$ -expressing tumors. *Mol Cancer Ther* 2015;14:1605–13.

38. Eaton JS, Miller PE, Mannis MJ, Murphy CJ. Ocular adverse events associated with antibody-drug conjugates in human clinical trials. *J Ocul Pharmacol Ther* 2015;31:589–604.
39. Zhao H, Atkinson J, Gulessarian S, Zeng Z, Nater J, Ou J, et al. Modulation of macropinocytosis-mediated internalization decreases ocular toxicity of antibody-drug conjugates. *Cancer Res* 2018;78:2115–26.
40. Kunkler AL, Binkley EM, Mantopoulos D, Hendershot AJ, Ohr MP, Kendra KL, et al. Known and novel ocular toxicities of biologics, targeted agents, and traditional chemotherapeutics. *Graefes Arch Clin Exp Ophthalmol* 2019;257:1771–81.
41. Moore KN, Borghaei H, O’Malley DM, Jeong W, Seward SM, Bauer TM, et al. Phase 1 dose-escalation study of mirvetuximab soravtansine (IMGN853), a folate receptor  $\alpha$ -targeting antibody-drug conjugate, in patients with solid tumors. *Cancer* 2017;123:3080–7.
42. Moore KN, Martin LP, O’Malley DM, Matulonis UA, Konner JA, Perez RP, et al. Safety and activity of mirvetuximab soravtansine (IMGN853), a folate receptor  $\alpha$ -targeting antibody-drug conjugate, in platinum-resistant ovarian, fallopian tube, or primary peritoneal cancer: a phase I expansion study. *J Clin Oncol* 2017;35:1112–8.
43. Matulonis UA, Birrer MJ, O’Malley DM, Moore KN, Konner J, Gilbert L, et al. Evaluation of prophylactic corticosteroid eye drop use in the management of corneal abnormalities induced by the antibody-drug conjugate mirvetuximab soravtansine. *Clin Cancer Res* 2019;25:1727–36.
44. Ab O, L.M.B., Lanieri L, Ponte JF, Qiu Q, Sikka S, Costopoulas JA, et al. A next generation folate receptor alpha targeting antibody drug conjugate active against tumors with low, medium and high receptor expression. *Cancer Res* 2020;80(16 Suppl):2890.
45. Luu KT, Bergqvist S, Chen E, Hu-Lowe D, Kraynov E. A model-based approach to predicting the human pharmacokinetics of a monoclonal antibody exhibiting target-mediated drug disposition. *J Pharmacol Exp Ther* 2012;341:702–8.
46. Dall’Acqua WF, Kiener PA, Wu H. Properties of human IgG1s engineered for enhanced binding to the neonatal Fc receptor (FcRn). *J Biol Chem* 2006;281:23514–24.
47. Junutula JR, Raab H, Clark S, Bhakta S, Leipold DD, Weir S, et al. Site-specific conjugation of a cytotoxic drug to an antibody improves the therapeutic index. *Nat Biotechnol* 2008;26:925–32.
48. Hamblett KJ, Senter PD, Chace DF, Sun MMC, Lenox J, Cerveny CG, et al. Effects of drug loading on the antitumor activity of a monoclonal antibody drug conjugate. *Clin Cancer Res* 2004;10:7063–70.
49. Strop P, Delaria K, Foletti D, Witt JM, Hasa-Moreno A, Poulsen K, et al. Site-specific conjugation improves therapeutic index of antibody drug conjugates with high drug loading. *Nat Biotechnol* 2015;33:694–6.
50. Cilliers C, Menezes B, Nessler I, Linderman J, Thurber GM. Improved tumor penetration and single-cell targeting of antibody-drug conjugates increases anticancer efficacy and host survival. *Cancer Res* 2018;78:758–68.